https://doi.org/10.48048/tis.2025.8897

Effective $CuSO_4$ Concentration on Phase Formation and Optical Characteristics of Electrodeposited Ni-Cu Alloy

Nuchjira Dejang[1], Arrak Klinbumrung[2,3] and Reungruthai Sirirak[2,3,*]

[1]Apply Physics Program, Department of Physics, Naresuan University, Phitsanulok 65000, Thailand
[2]Unit of Excellence on Advanced Nanomaterials, University of Phayao, Phayao 56000, Thailand
[3]School of Science, University of Phayao, Phayao 56000, Thailand

([*]Corresponding author's e-mail: reungruthai.si@up.ac.th)

Received: 29 August 2024, Revised: 14 September 2024, Accepted: 16 October 2024, Published: 20 November 2024

Abstract

Ni-Cu alloys play a critical role in various industrial applications due to their exceptional characteristics. Despite extensive study of these alloys for their mechanical and corrosion characteristics, their optical properties have received limited attention. In this research, the electrodeposition of Ni-Cu alloy coatings was conducted using copper sulfate concentrations ranging from 1.25 to 10 g/L, leading to successful film formation with various phases. XRD examination associated with the Rietveld calculation exhibited modified phase fraction, crystallite size, micro-strain, and lattice constant. Scanning Electron Microscopy (SEM) analysis revealed a different thickness and a dendritic microstructure. As an increase in $CuSO_4$, there was observed an increase in the values of the absorption edge (showing 1.61 - 1.90 eV), texture coefficient (0.46 - 0.82), and film thickness (0.63 - 1.74 µm). These various morphologies enhanced the material's properties. In more added $CuSO_4$ samples, the coatings significantly reveal a modification in the crystal, film growth, and optical properties. The advancements in visible light absorption suggest an enhanced coating for optical technology applications.

Keywords: Ni-Cu Alloy, Film, Electrodeposition, Phase formation, Optical characteristics, X-ray diffraction, Scanning Electron Microscopy

Introduction

Intermetallic compounds are currently extensively explored due to their significance in various applications, such as high-temperature applied materials, corrosion resistance, catalytic activity, heat exchangers, and hydrogen storage materials [1-5]. Nickel-copper (Ni-Cu) compounds, illustrated as Monel alloy, are highly valued in industrial settings for their excellent mechanical properties and corrosion resistance due to the face-centered cubic (FCC) arrangement of nickel and copper, creating alloys with diverse ratios and superior wide-range applications [6,7].

Besides the mechanical and corrosion studies, the related optical characteristics of Ni-Cu alloy were also attractive to determine due to the usage of the materials in high temperatures and the surrounding corrosion. As found in the previous reports, Ni-Cu alloy films have been extensively examined for insight into their optical performances. The optical density (D_{opt}) and skin depth (δ) of carbon nanotubes on Ni-Cu films were modified by displaying the greatest skin depth (190 nm for 0 % Cu content) and the optical density (up to 75 % for 5 % Cu content) [8]. Additionally, the correlation between the energy band gap and Urbach energy indicates that the energy band gap decreases with increased Urbach energy [8]. This finding concludes that Cu incorporation in the Ni-Cu compound influences the optical properties.

Moreover, Ni and Cu co-catalysts on TiO_2 nanotubes show that a 1:1 Ni:Cu atomic ratio in a 10 nm-thick film yields the highest photocatalytic hydrogen evolution rate, demonstrating a synergistic effect between Ni and Cu [9]. Dendrite-structured Ni-Cu alloys prepared at 140 °C exhibit excellent electromagnetic-wave absorption properties with a reflection loss of –31.13 dB at 14.3 GHz and an adjustable effective absorption bandwidth between 4.4

and 18 GHz [10]. As mentioned above, Ni-Cu alloy exhibits an attractive photo-responsibility, introducing the potential for applications in optical technologies.

Innovative alloy coatings were described using several techniques [11]. For Ni-Cu alloy, this film was also grown using various preparation processes. The use of complex agents such as pyrophosphate, citrate, acetate, sulfa-mate, and glycine is crucial to minimize the difference between nickel (Ni) and copper (Cu) in alloy compositions [12]. Ghosh *et al*. [13] and Dai *et al*. [14] studied the effects of different compositions on the electrochemical properties and microstructural characteristics of Ni-Cu films, discovering the relation between the alloying elements and performance metrics. Furthermore, Goranova *et al*. [15] investigated the impact of pH and salt concentrations on the crystallographic structures of Ni-Cu alloys. Among the preparation processes, the electrodeposition process is recognized as a cost-efficient and adaptable technique for creating porous metals and metallic alloys [16,17]. By the potential adjustment, the process can synthesize porous films on conductive substrates with pore sizes spanning from meso- to micron-scale [19]. The critical factors influencing the size of the pores are the choice of template, the electrolyte formulation, and the film growth rate [20]. Consequently, the preparing route with different parameters affects the properties of Ni-Cu coatings.

In this study, Ni-Cu films with different Cu atomic fractions were prepared by utilizing the electrodeposition technique. To our knowledge, the literature lacks reports on the optical characteristics of Ni-Cu films, which were studied by various Cu^{2+} concentrations. The quantity of copper content in Ni-Cu compounds influences the phase, crystal, and optical properties. Therefore, the phase formation, morphology, and optical characteristics were analyzed and discussed to understand their impact on material application.

Materials and methods

Material preparation

To prepare the Ni-Cu alloy coating, the film was deposited using the electrodeposition technique. The sulfate-based electrolytes comprise 0.1 M of $NiSO_4$ solution incorporated by the various concentrations of $CuSO_4$ (1.25, 2.5, 5.0, 7.5, and 10 g/L). The cleaned stainless-steel plates (SST 440) of 2 cm^2 (2×1 cm^2) were used as a cathode. The nickel plate, which was similar in size and performed as an anode electrode, was placed at a 3 cm length from the cathode. For each deposition batch, the DC potential of 2.1 V was applied for 60 min. After the deposition, the as-received coating was washed with DI water, dried, and then stored in a desiccator cabinet.

Characterization

To determine the structural characteristics of the synthesized materials, X-ray diffractometer analysis (XRD, Bruker model D2Phaser) was employed using Cu Kα radiation (λ = 0.154059 nm) by measuring the 2θ in the range of 30 - 70 ° with the step of 0.01 °. The morphology of the deposited coating was determined through a scanning electron microscope (SEM, JEOL model JSM-6335F), operating at 15 kV with energy-dispersive X-ray analysis (EDX) to examine the elemental distribution. The optical properties were analyzed using a UV-Vis spectrophotometer (Jasco, V-503) in the 400 - 800 nm spectrum range. The absorbance was measured to determine the optical and structural characteristics, and their optical functions were further calculated, including textured coefficients, skin depth, optical density, extinction coefficients, and refraction index. The as-synthesized coatings were assigned as the 1.25Cu-Ni, the 2.5Cu-Ni, the 5.0Cu-Ni, the 7.5Cu-Ni, and the 10Cu-Ni for the prepared conditions with the various $CuSO_4$ concentrations of 1.25, 2.5, 5.0, 7.5, and 10 g/L, respectively.

Results and discussion

X-ray diffraction analysis was conducted on the coatings prepared using various concentrations of $CuSO_4$ (1.25, 2.5, 5.0, 7.5, and 10 g/L) in a 0.1 M solution of $NiSO_4$ electrolyte, as illustrated in **Figure 1**. The diffractogram was observed at 2θ degrees in the range of 30 - 80 °. The crystal planes are in correspondence with copper (Cu, JCPDS #03-1018), nickel (Ni, JCPDS#87-0712), iron (Fe, JCPDS #87-0722), and $Cu_{0.81}Ni_{0.19}$ alloy (JCPDS #47-1406). The prominent peaks of all phases appear at the closed position due to their formation in the cubic crystal structure, leading to difficulty in identifying phases. Therefore, the Rietveld method was employed to analyze the XRD data to determine phase formation and

structural values, including some physical properties [21]. Herein, the refinement calculations were conducted using the MAUD software package [22] and the Crystallographic Information File (CIF) from the Crystallography Open Database (COD). According to their space groups, the CIF numbers for Cu, Ni, and Fe crystal structures are 5000216, 9012034, and 5000217, respectively. For the $Cu_{0.81}Ni_{0.19}$, the crystal information was generated using the dataset presented as JCPDS #47-1406, giving a space group of Fm3m and a lattice length of 3.5934 Å.

In association with the approximation by the Rietveld method, the phase formation and physical properties, including crystallite size, micro-strain, and lattice constants, were determined. After completing the refinement cycle, the statistical parameter values for the R experiment (R_{exp}) and the goodness of fit (Sig) over $CuSO_4$ contents from 1.25 to 10 g/L were found to be 1.9893, 8.4427, 8.1503, 6.2558, and 6.5038 % (for R_{exp}) and 1.9897, 1.3189, 3.7435, 1.5558, and 1.8244 (for Sig). These quantities are revealed to validate the appropriate fitting. This finding indicates that both R_{exp} and Sig values for all samples are below 10 %, indicating a reliable refinement process [23]. As depicted in **Figure 1(a)**, the 1.25Cu-Ni existed the phase of $Cu_{0.81}Ni_{0.19}$ (28.96 wt%) and Fe (71.04 wt%). The trace amount of Cu was found in the 2.5Cu-Ni. As $CuSO_4$ was added more than 2.5 g/L, the strong crystal plan at around 44 ° clearly divides into 2 peaks, introducing the (111) crystal plan of Cu and $Cu_{0.81}Ni_{0.19}$ present at 43 °. The pattern of the 5.0 Cu-Ni is similar to that of the 7.5Cu-Ni. Considering the weight ratio of $Cu_{0.81}Ni_{0.19}$ alloy, the fraction is 30.14, 33.72, and 59.45 wt% for the 2.5Cu-Ni, the 5.0Cu-Ni, and the 7.5Cu-Ni, respectively. The stronger signal to refer to the Cu, and $Cu_{0.81}Ni_{0.19}$ crystals plan was investigated as more $CuSO_4$ incorporation, indicating the higher crystallinity. The 10Cu-Ni reveals the phases of $Cu_{0.81}Ni_{0.19}$ (29.07 wt%), Cu (9.20 wt%), Ni (16.62 wt%), and Fe (45.11wt%). The effect appeared that the Cu phase separated from the $Cu_{0.81}Ni_{0.19}$ alloy. According to the literature, Cu^{2+} ion has more electrochemical properties than Ni^{2+}. The significant variance in the standard reduction potential between Cu (+0.34 V) and Ni (–0.25 V) results in Cu^{2+} being reduced more rapidly than Ni^{2+} [24]. This results in easier growth of copper crystals during the electrochemical deposition process. As mentioned, this may cause some Cu^{2+} ions to grow and nucleate spontaneously, leading to the nucleation of some Ni^{2+} ions in a comparable pathway. Interestingly, as shown in the JCPDS database, the 2θ of (111) crystal plane Ni and Fe structures reveals a very close position, showing at 44.5 ° for Ni and 44.8 ° for Fe. Note that Ni phase may form in other conditions besides the 10 Cu-Ni.

Owing to its prominent phase, the evolution of the $Cu_{0.81}Ni_{0.19}$ phase can be discussed in relation to other components. Thus, **Table 1** shows the estimated crystallite size, micro-strain, and lattice constant of the phase. As increasing $CuSO_4$ concentration, the values of crystallite size (exhibiting 25.80, 45.98, 164.91, 367.20, and 295.12 nm), micro-strain (giving ($*10^{-4}$): 83.607, 69.163, 93.808, 53.751, and 15.296), and lattice constant (giving 3.568, 3.585, 3.583, 3.608, 3.610 Å) correspond to the phase formation. The largest crystallite size in the 7.5 Cu-Ni indicates the lowest intrinsic defects hindering crystal growth, associated with the lowest micro-strain (in comparison to conditions of the copper segregation). As found in the 10Cu-Ni, Cu and Ni appearance reduces residual strain. The increase in the lattice parameter of the Ni-Cu alloy with the rise in Cu concentration can be attributed to the larger size of Cu atoms compared to Ni. This is because the atomic radius of Cu is 0.128 nm while that of Ni is 0.124 nm [25]. The increasing lattice parameter of $Cu_{0.81}Ni_{0.19}$ with an increase in Cu atomic percentage is associated with the expectations outlined by Vegard's law. Moreover, in the 7.5Cu-Ni, the lattice constant is most similar to the JCPDS value, which was 3.593 Å, confirming the superb atomic arrangement of the $Cu_{0.81}Ni_{0.19}$ phase.

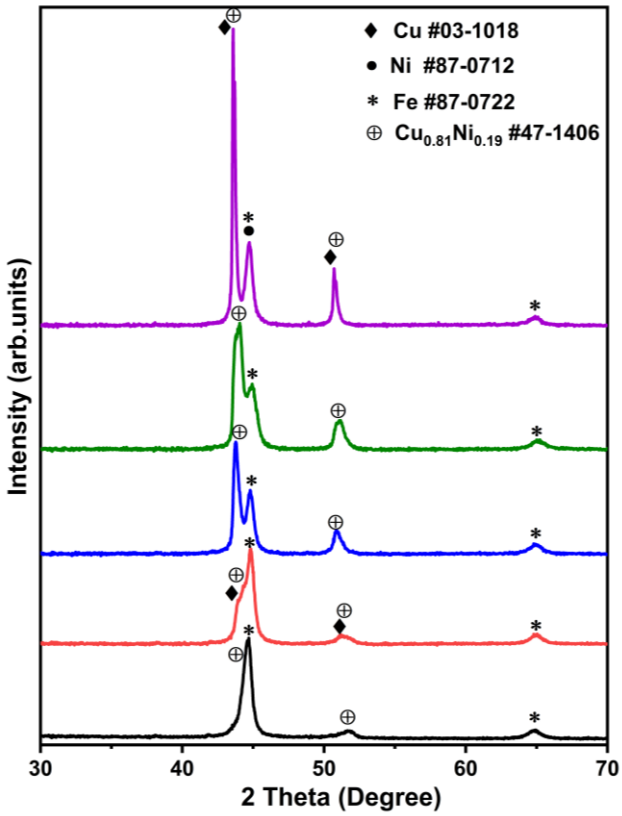

Figure 1 The XRD pattern of (a) the 1.25Cu-Ni, (b) the 2.5Cu-Ni, (c) the 5.0Cu-Ni, (d) the 7.5Cu-Ni, and (e) the10Cu-Ni.

Table 1 The structural and statistical values of the as-prepared coating calculated by the Rietveld refinement.

Samples	Phases (wt%)	Approximated values of $Cu_{0.81}Ni_{0.19}$ phase			R's	
		Crystallite Size (nm)	Micro-strain ($*10^{-4}$)	Lattice constants (Å)	R_{exp} (%)	Sig (%)
1.25Cu-Ni	$Cu_{0.81}Ni_{0.19}$ = 28.96 Fe = 71.04	25.80	83.607	3.568	1.9893	1.9897
2.5Cu-Ni	$Cu_{0.81}Ni_{0.19}$ = 30.14 Cu = 0.25 Fe = 69.61	45.98	69.163	3.585	8.4427	1.3189
5.0Cu-Ni	$Cu_{0.81}Ni_{0.19}$ = 33.72 Fe = 66.27	164.91	93.808	3.583	8.1503	3.7435
7.5Cu-Ni	$Cu_{0.81}Ni_{0.19}$ = 59.45 Fe = 40.55	367.20	53.751	3.608	6.2558	1.5558
10Cu-Ni	$Cu_{0.81}Ni_{0.19}$ = 29.07 Cu = 9.20 Ni = 16.62 Fe = 45.11	295.12	15.296	3.610	6.5038	1.8244

In material crystallography, the tendency of a material to align itself in a particular direction and establish a crystallized texture is identified as the preferred alignment. The presence of a texture coefficient (TC) in a material indicates whether there are random orientations of crystallites (TC_{hkl} = 1) or a preference for a specific orientation (TC > 1) along a particular (hkl) direction [26]. The value of the TC reflects the degree of alignment of crystallites. A specific equation calculates this parameter, quantifying the degree of preferred orientation in crystalline materials [27].

$$TC = \frac{N(I_{hkl})/(I_{0_{hkl}})}{\sum_n (I_{hkl})/(I_{0_{hkl}})} \quad (1)$$

where the specific plan's intensity (I_{hkl}) is compared with the standard intensity ($I_{0_{hkl}}$) as exhibited in the JCPDS cards. N represents the total reflections, and n is the number of diffraction peaks. The crystal plan of (111) was analyzed using the texture coefficient function to understand its crystallinity. As shown on **Table 2**, the TC values of the 1.25Cu-Ni, the 2.5Cu-Ni, the 5.0Cu-Ni, the 7.5Cu-Ni, and the10Cu-Ni are 0.46, 0.48, 0.77, 0.77, and 0.82, respectively. The quantity interprets the low crystallinity due to the value below 1 in all samples. Nevertheless, the observed amount shows an increasing tendency, concluding that the $CuSO_4$ concentration directly affects crystallinity.

Table 2 The calculated $TC_{(111)}$ of $Cu_{0.81}Ni_{0.19}$, film thickness, and some optical function values of the as-prepared Ni-Cu coatings.

Samples	$TC_{(111)}$ values of $Cu_{0.81}Ni_{0.19}$ phase	Film thickness (μm)	Absorption edge (nm)	*k* value at 550 nm (*10^{-6})	*n* value at 550 nm
1.25Cu-Ni	0.46	0.63	770	7.357	0.29
2.5Cu-Ni	0.48	0.65	720	8.887	0.37
5.0Cu-Ni	0.77	1.36	660	9.799	0.42
7.5Cu-Ni	0.77	1.54	652	9.985	0.45
10Cu-Ni	0.82	1.74	652	9.985	0.45

The cross-sectional scanning electron microscopy (SEM) images illustrating the prepared coatings are presented in **Figure 2**. Fundamentally, in the metal electrodeposition process, the reduction of metal ions on the substrate leads to stable clusters formed by adsorbed atoms. Incorporating more $CuSO_4$ enhances the metal ion concentration, increases surface mobility, and influences the coating's grain size and microstructure. The microstructure of these coatings reveals a dense arrangement of small granular clusters. When the concentration of $CuSO_4$ is less than 7.5 g/L, these clusters appear as thin, elongated platelets that are evenly dispersed over the surface (**Figures 2(a)-2(c)**). Nucleation can be attributed to growth mechanisms, which facilitate the aggregation of discrete islands into a 2-dimensional layer, with lateral grain size influenced by supersaturation levels and surface mobility of adsorbed materials [28]. Investigating the 7.5Cu-Ni and the 10Cu-Ni, the solidification structure remains as equiaxed crystals. There is a noticeable change in the grain morphology. Polygonal structures with an increasing particle size exhibit a distinct growth pattern, as displayed in **Figure 2(d)**. The 10Cu-Ni (**Figure 2(e)**) reveals larger irregular particles with a wide size distribution (about 50 - 700 nm), confirming an impact of $CuSO_4$ amount on the crystal growth mechanisms. In correspondence with the previous elemental analysis on electrodeposited Ni-Cu coating [29], the equiaxed particle film was found in the higher Cu atomic percentile (55.812 at % for Ni and 44.188 at % for Cu). In contrast, the conditions with a component of 88.017 at % of Ni and 11.983 at % of Cu show a dense and elongated particle film. Due to an electrodeposition process, the film is formed through a layer-growth mechanism. Therefore, the chemical components are a vertical distribution [30]. The 10Cu-Ni with a larger particle is plausible to form various phases in each deposited layer. As found in the 10Cu-Ni, a high amount of Cu is not conducive to forming Ni-Cu alloys. Due to a higher concentration of Cu^{2+}, Cu crystal growth on the surface also leads to Ni growth [31]. The growth mechanism of the Cu-Ni compound at a temperature higher than 240 K was described due to a high number of annealing twins [25]. The random orientation in the microstructure is attributed to stress fractures of the primary dendrite network. An alloy with an irregular shape can be described as a rapidly solidified and randomly oriented structure. Influencing Cu concentration on larger particle size, the deposited particle size tends to increase, attributing to the

enhanced electrodeposition rate, which results in larger particles forming on the substrate [32]. The study reveals the particle size of 5.5 µm with needle tip when Cu concentration is 90 g/L. Due to faster deposition, higher Cu^{2+} conditions present a longitudinal growth. Similar to this work, under low Cu^{2+} conditions, copper ions assemble at the beginning of the grain, causing the grains to enlarge and a decrease in copper ions at the base of the grain. The larger grain size makes it easier for copper ions to be discharged and deposited, making the deficiency of copper ions at the base of the grain. This finding confirms that the Cu^{2+} concentration affects the surface particle growth. The morphology of Cu-Ni alloys changes with varying Cu concentrations. Higher Cu concentrations lead to a transition from a wavy layered structure to a nodular structure, indicating a significant impact on the microstructural distribution [33].

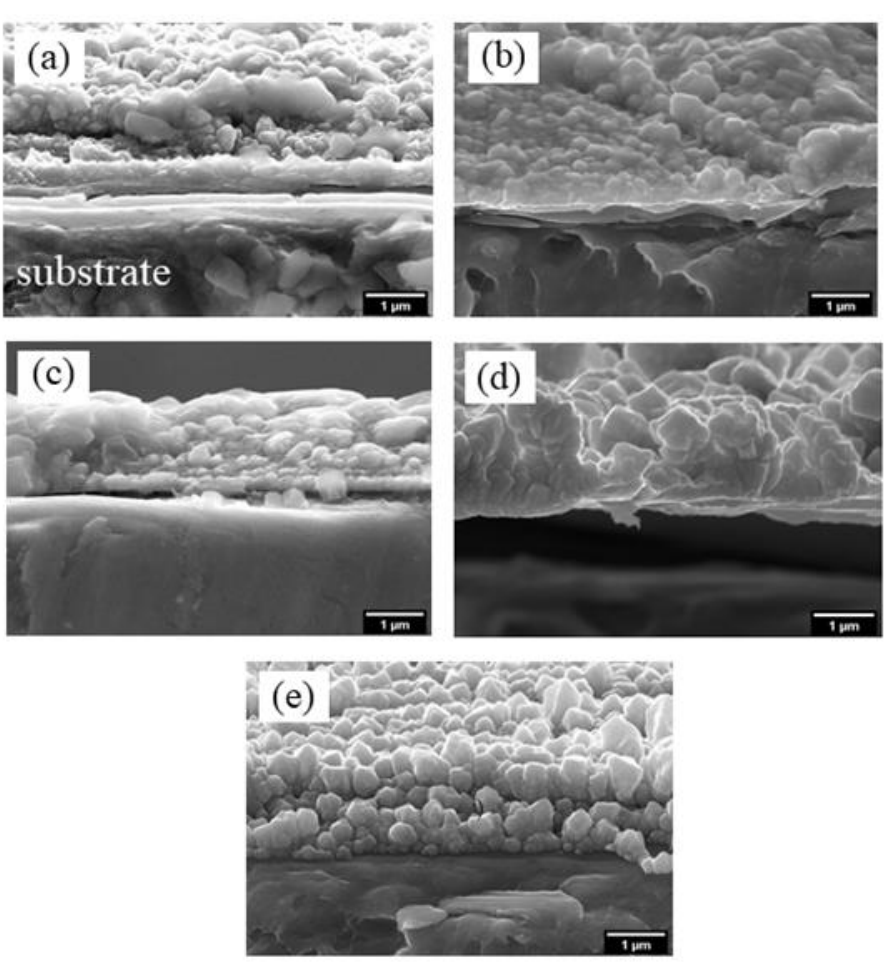

Figure 2 SEM micrograph of the cross-section Ni-Cu coating: (a) the 1.25Cu-Ni, (b) the 2.5Cu-Ni, (c) the 5.0Cu-Ni, (d) the 7.5Cu-Ni, and (e) the10Cu-Ni.

The scanning electron microscopy (SEM) images were evaluated through the image J software to determine the thickness of the coatings, as demonstrated in **Table 2**. The results show a rise in coating thickness with an increasing $CuSO_4$ concentration, found to be 0.63, 0.65, 1.36, 1.54, and 1.74 µm. The higher $CuSO_4$ concentration encourages the formation of dendritic structures. The Ni-Cu alloy coatings exhibited an island growth (or Volmer-Weber) mechanism [34]. The aggregation of large particles contributes to an increase in coating thickness.

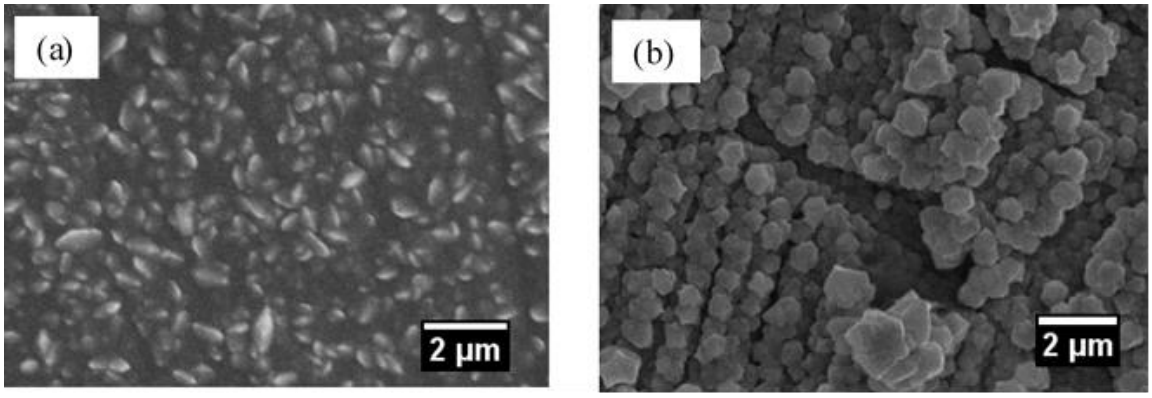

Figure 3 The SEM images observed the morphology of the coating's surface, showing (a) the 1.25Cu-Ni and (b) the 10Cu-Ni.

The surface morphology of the coatings is further depicted in **Figure 3**. **Figure 3(a)** displays the morphology of the 1.25Cu-Ni, revealing small, elongated, plate-like particles. In contrast, the coating generated in the 10Cu-Ni shows well-defined polygon-shaped grains (**Figure 3(b)**). This difference in morphology is associated with variations in the Cu content of the coatings. As depicted in **Figure 4**, the energy-dispersive X-ray spectroscopy (EDS) examination of the coatings validates the steady distribution of Ni and Cu atoms on the surface of the 10Cu-Ni.

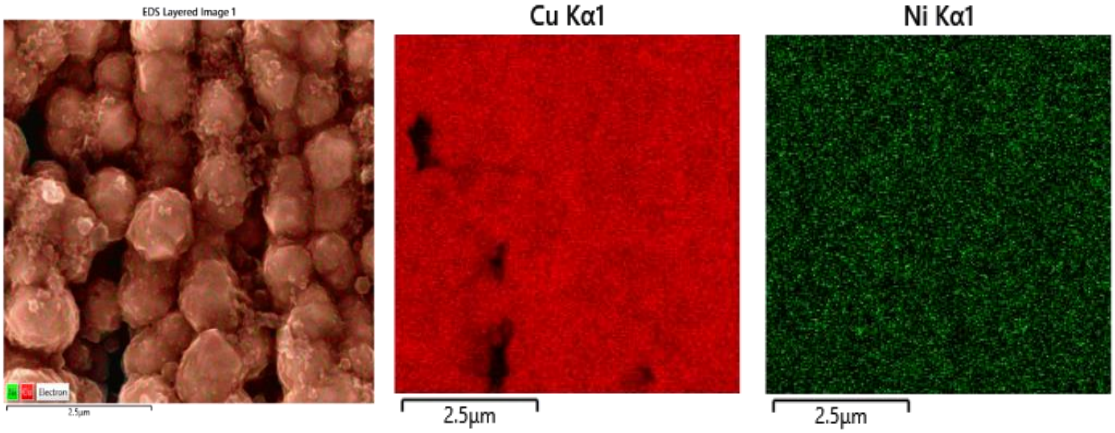

Figure 4 The elemental distribution of Cu and Ni on the 10Cu-Ni's surface was investigated using energy-dispersive X-ray spectroscopy (EDS).

The UV-visible absorbance of the Ni-Cu coating is presented in **Figure 5**. As observed, all samples respond to the shorter wavelength spectrum (higher energy) more than that of the longer wavelength spectrum (lower energy). The enhanced absorbance intensity is attributed to the sufficient excitation energy, resulting in an increased concentration of free electrons [35]. The absorption edge observed in Ni-Cu alloys signifies a distinct energy level or wavelength, which suddenly rises in electromagnetic radiation absorption, indicating that electrons elevate from lower to higher energy states. To determine the absorption edges, the linear portion (dashed line as presented in **Figure 5**) was extrapolated to absorbance approach 0. The absorbed wavelength can be changed to the photon energy (E photon, eV) using the relation [36].

$$E_{photon} = \frac{1240}{\lambda} \quad (2)$$

The absorption edges of the Ni-Cu coating are 770 nm (1.61 eV), 720 nm (1.72 eV), 660 nm (1.88 eV), 652 nm (1.90 eV), 652 nm (1.90 eV) when $CuSO_4$ content of 1.25, 2.5, 5.0, 7.5, and 10 g/L, respectively. The

absorption peaks were observed at around 375 nm, corresponding with the report of Wu *et al*. [36], which showed an absorption of 400 nm [37]. The absorbance intensity can be attributed to the defects in the lattice. In Ni-Cu alloys, defects significantly affect energy absorption characteristics by altering charge redistribution. Following the previous study as a result of XANES spectra. The observed 3-peak feature at the Cu L_3-edge indicates that increased Cu content results in a shift to higher photon energy, influencing the d charge rehybridization of both Cu and Ni [38]. Consequently, this electronic structural modification, particularly the movement of d bands towards the Fermi level, enhances the energy absorption properties of the alloy [38]. The emerging defects can be considered a vital reason for the absorption edge shift to the higher energy. More, surface plasmon resonance was reported at around 600 nm [39], introducing an absorption in the 7.5Cu-Ni and the 10Cu-Ni. At below 600 nm, the 7.5Cu-Ni and the 10Cu-Ni show significant absorbance with similar capabilities. On the contrary, insignificant spectrum absorbance was found in the 1.25Cu-Ni. This increase in absorbance is caused by the light scattering at the grain boundary, as demonstrated in a prior study [40]. This study exhibits the most absorbance in a more significant particle film forming in the vertical direction. Owing to the difference in morphology, it can be supposed that the cavity along the crystal growth direction acts as an absorption center.

The amount of energy absorbed by a substance depends on several factors, including the extinction coefficient, material composition, conductivity, and thickness in the absorption area. The absorption coefficient (α) of incident photon energy was considered as a result of the skin depth (δ), which was calculated using Eq. (3) [41].

$$\text{Skin depth } (\delta) = 1/\alpha \quad (3)$$

The relationship between skin depth (δ) and photon energy (hv) shows a decreasing δ value as photon energy increases (**Figure 6**). This phenomenon describes that a higher-frequency spectrum (higher energy) deeply travels into materials. According to the absorbance study, the 1.25Cu-Ni unveils the least absorbance. When travelling through the material, a small portion of the incident light is absorbed, resulting in the extension of the light pathway.

The optical density (D_{opt}) measures light intensity attenuation when the light travels through a material. A higher optical density means more light is absorbed, while a lower optical density means more light can pass through. To calculate the D_{opt} value, an equation is presented in Eq. (4) [42]. Where α represents the absorption coefficient and t replies to the thickness (1 cm).

$$D_{opt} = \alpha t \quad (4)$$

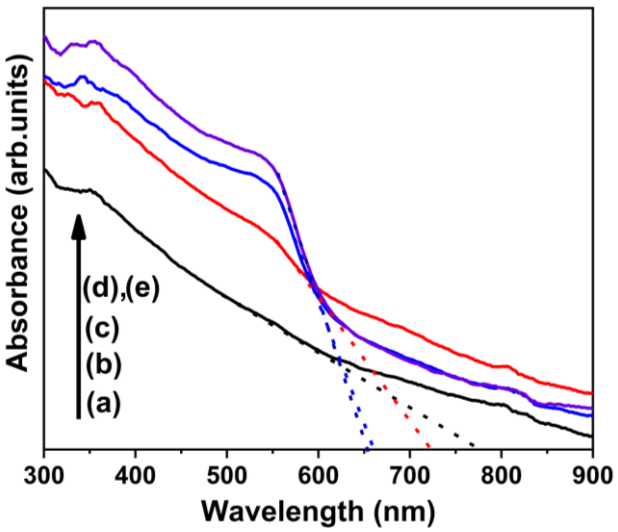

Figure 5 The UV-visible absorbance of (a) the 1.25Cu-Ni, (b) the 2.5Cu-Ni, (c) the 5.0Cu-Ni, (d) the 7.5Cu-Ni, and (e) the10Cu-Ni.

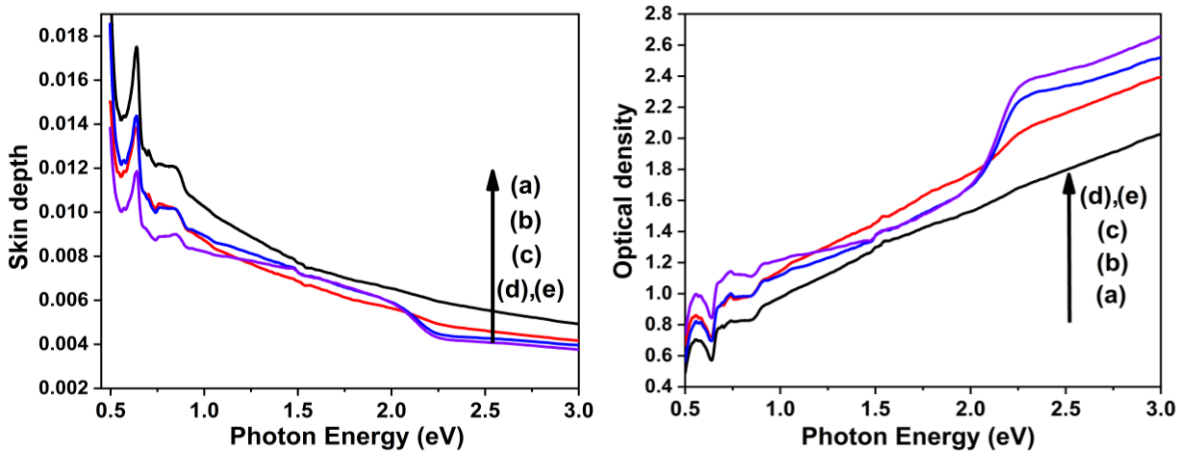

Figure 6 The skin depth and optical density of (a) the 1.25Cu-Ni, (b) the 2.5Cu-Ni, (c) the 5.0Cu-Ni, (d) the 7.5Cu-Ni, and (e) the 10Cu-Ni.

Considering the plotting in **Figure 6**, the D_{opt} value demonstrates an inverse trend compared to the skin depth. This relation suggests that light travels deeply into the substance, introducing a low optical density. As a result, the 7.5Cu-Ni and the 10Cu-Ni showed the most absorbance compared to coatings. These materials also present the highest optical density. In addition to the advantages mentioned, the observation promises the potential for their utilization in light attenuation processes.

The extinction coefficient (k) is a critical parameter in optical investigations, elucidating the absorption of electromagnetic waves within a medium. Decreasing absorption results in scattering phenomena. Understanding the behavior of light-matter interaction and its impact on the propagation of light through different materials relies on determining the extinction coefficient (k). The coefficient is influenced by the complex relationship of absorption, scattering, and other phenomena, affecting the optical properties of the material. The related equation is presented as follows [43].

$$k = \alpha\lambda/4\pi \quad (5)$$

The relationship between the wavelength of incident photons (λ) and the absorbance coefficient (α) directly influences the extinction coefficient change. As the wavelength (λ) increases, the parameter "k" also increases, resulting in the light loss due to a higher scattering rate. Considering a peak placed at the wavelength of 550 nm, the end of the absorption linear portion, the *k* values ($*10^{-6}$) are 7.357, 8.887, 9.799, 9.985, 9.985 for $CuSO_4$ content of 1.25 - 10 g/L, respectively. At a wavelength lower than the absorption edge wavelength, the k value of the 5 - 10 g/L $CuSO_4$ content became lower than the 2.5Cu-Ni. This causes photon energy to be not enough to excite the electron. The lowest k value in the 1.25Cu-Ni may cause the most insignificant thickness, resulting in the lowest photon absorption. Compared with the 81 vol% Cu with a diameter of 4.4 nm, the k value was presented at around 575 nm [44]. This study shows that more energy excitation may influence various phase combinations.

The refractive index (n) is a vital optical parameter that meaningfully impacts the progress of optical tools in analysing the polarization phenomena and phase velocity of light in materials. The determination of the refractive index is achieved through the utilization of Eq. (6) [45].

$$n = \frac{1}{T_s} + \left(\frac{1}{T_s - 1}\right)^{\frac{1}{2}} \quad (6)$$

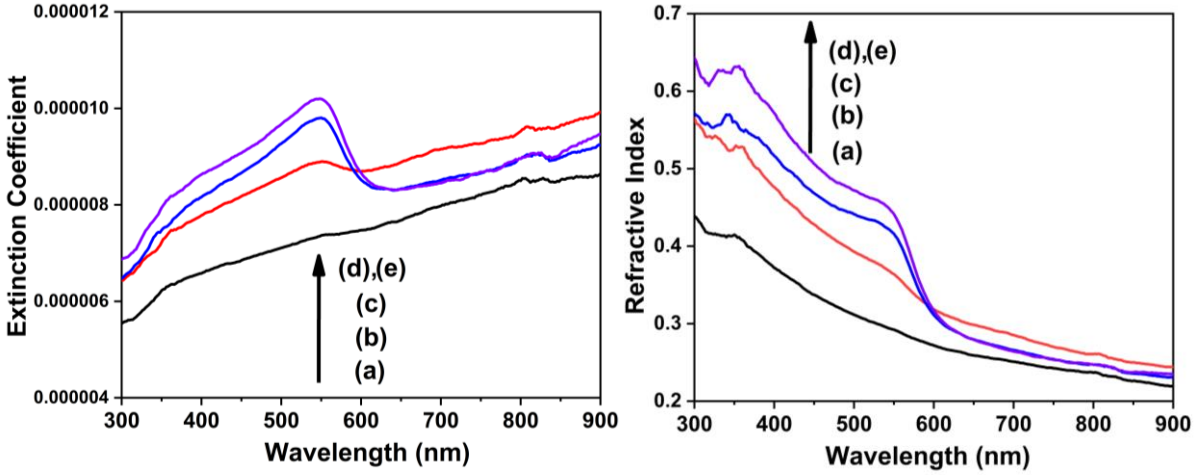

Figure 7 The extinction coefficient and refractive index of (a) the 1.25Cu-Ni, (b) the 2.5Cu-Ni, (c) the 5.0Cu-Ni, (d) the 7.5Cu-Ni, and (e) the 10Cu-Ni.

As depicted in **Figure 7**, the relationship between refractive index and wavelength illustrates a significant trend. Higher refractive index values are observed within the $300 < \lambda < 550$ nm absorption range owing to the adequate exciting energy for electronic transitions. At the wavelength of 550 nm, the refractive index values are 0.29, 0.37, 0.42, 0.45, and 0.45 over the added $CuSO_4$ condition of 1.25 - 10 g/L. On the other hand, the lower activation energy leads to a systematic decrease in the refractive index [46]. The refractive index increases as the absorption increases. Increasing $CuSO_4$, these peaks slightly shifted towards shorter wavelengths, corresponding with the absorbance analysis. As a result, the 7.5Cu-Ni and the 10Cu-Ni exhibit a greater *n* value when the activating energy is proper to drive electrons across the energy state. The finding can be interpreted as the light trapping in the material, confirming visible light absorption capability.

Conclusions

The electrodeposition of Ni-Cu coatings using varying concentrations of copper sulfate ($CuSO_4$) from 1.25 to 10 g/L successfully prepared as resulted in the formation of Cu, Ni, Fe, and $Cu_{0.81}Ni_{0.19}$. Owing to the more positive standard reduction potential of Cu^{2+}, the increasing Cu^{2+} concentration in the electrolyte promoted enhanced interaction between Ni^{2+} and Cu^{2+} ions, leading to a higher proportion of the $Cu_{0.81}Ni_{0.19}$ phase. The 7.5 Cu-Ni demonstrates a close lattice constant value to the JCPDS database, resulting in a significant crystallite size with low micro-strain. Determining the 7.5Cu-Ni and the 10Cu-Ni, SEM analysis reveals the high thickness and the distinctive dendritic microstructure. With the advantage in the optical functions, the dendritic microstructure with vertical growth improves the absorbance, optical density extinction coefficient, and refractive index. The increasing absorption edges of the Ni-Cu coating were found in the range of 1.61 - 1.90 eV when $CuSO_4$ content of 1.25 - 10 g/L, causing increased Cu L_3-edge due to Cu content resulting in a shift to higher photon energy. As an increase in $CuSO_4$, the growing values of absorption edge, texture coefficient, showing 0.46 - 0.82, and film thickness, 0.63 - 1.74 µm, can be supposed to the development of the crystal, film growth, and optical properties. In conclusion, the electrodeposited Ni-Cu coatings prepared in the route of the 7.5Cu-Ni expose better quality in structural and optical properties compared with those of samples. The coating with a superior absorption at 550 nm (*k* values of 9.985×10^{-6}) and *n* value of 0.45 can be considered a visible light absorption material with anti-corrosion properties. This coating demonstrates a promising potential for applications in related optical technology.

Acknowledgements

This research was funded by Thailand Science Research and Innovation (TSRI) under grant number FF66-RIM018. We would also like to acknowledge the financial support provided by Naresuan University

through research project No. R2565B065. Additionally, we are grateful to the Unit of Excellence on Advanced Nanomaterials and the School of Science, University of Phayao, Thailand, for their support.

References

[1] RS Yang, MT Li, CH Liu, XJ Cui and YZ Jin. The synthesis of $Cu_{0.81}Ni_{0.19}$ intermetallics by mechanical alloying. *Advanced Materials Research* 2012; **496**, 379-382.

[2] X Wang, J Bai, M Zhang, Y Chen, L Fan, Z Yang, J Zhang and R Guan. A comparison between porous to fully dense electrodeposited CuNi films: Insights on electrochemical performance. *Nanomaterials* 2023; **13(3)**, 491.

[3] E Casado-Rivera, DJ Volpe, L Alden, C Lind, C Downie, T Vázquez-Alvarez, ACD Angelo, FJ DiSalvo and HD Abruña. Electrocatalytic activity of ordered intermetallic phases for fuel cell applications. *Journal of the American Chemical Society* 2004; **126(12)**, 4043-4049.

[4] R Solmaz, A Döner and G Kardaş. Electrochemical deposition and characterization of NiCu coatings as cathode materials for hydrogen evolution reaction. *Electrochemistry Communications* 2008; **10(12)**, 1909-1911.

[5] W Jesus, V Silva, H Souza, T Costa, O Rocha, L Nascimento and A Silva. Thermal and microstructural characterization of the multicomponent alloy Al33wt%Cu1wt%Ni-1.2 wt%Ta solidified with transient heat flow. *Trends in Sciences* 2024; **21(9)**, 8029.

[6] GN Flint and CP Cutler. *Nickel metal and alloys*. *In*: JJ Hostynek and HI Maibach (Eds.). Nickel and the skin: Absorption, immunology, epidemiology, and metallurgy. CRC Press, Florida, 2002, p. 219-238.

[7] KRM Rao. *Corrosion resistance of high entropy alloys*. *In*: K Kumar, BS Babu and JP Davim (Eds.). Coatings: Materials forming, machining and tribology. Springer, Cham, Switzerland, 2021, p. 81-115.

[8] V Dalouji and S Goudarzi. MWNTs on NiCu-a-C: H substrates: Study of optical linear equations, optical density, steepness and electron-phonon interaction. *Molecular Crystals and Liquid Crystals* 2022; **746(1)**, 79-92.

[9] M Pinna, AWW Wei, D Spanu, J Will, T Yokosawa, E Spiecker, S Recchia, P Schmuki and M Altomare. Amorphous NiCu thin films sputtered on TiO_2 nanotube arrays: A noble-metal free photocatalyst for hydrogen evolution. *ChemCatChem* 2022; **14(23)**, e202201052.

[10] B Zhao, W Zhao, G Shao, B Fan and R Zhang. Morphology-control synthesis of a core-shell structured NiCu alloy with tunable electromagnetic-wave absorption capabilities. *ACS Applied Materials & Interfaces* 2015; **7(23)**, 12951-12960.

[11] K Tewari, D Thapliyal, CK Bhargava, S Verma, A Mehra, S Rana, AK Gautam, GD Verros and RK Arya. *Innovative coating methods for industrial applications*. *In*: RK Arya, GD Verros and JP Davim (Eds.). Functional coatings: Innovations and challenges. John Wiley & Sons, New Jersey, 2024, p. 23-50.

[12] SM Silaimani, G Vivekanandan and P Veeramani. Nano-nickel-copper alloy deposit for improved corrosion resistance in marine environment. *International Journal of Environmental Science and Technology* 2015; **12**, 2299-2306.

[13] SK Ghosh, AK Grover, GK Dey and MK Totlani. Nanocrystalline Ni-Cu alloy plating by pulse electrolysis. *Surface and Coatings Technology* 2000; **126(1)**, 48-63.

[14] PQ Dai, C Zhang, JC Wen, HC Rao and QT Wang. Tensile properties of electrodeposited nanocrystalline Ni-Cu alloys. *Journal of Materials Engineering and Performance* 2016; **25(2)**, 594-600.

[15] D Goranova, R Rashkov, G Avdeev and V Tonchev. Electrodeposition of Ni-Cu alloys at high current densities: Details of the elements distribution. *Journal of Materials Science* 2016; **51**, 8663-8673.

[16] D Li and EJ Podlaha. Template-assisted electrodeposition of porous Fe-Ni-Co nanowires with vigorous hydrogen evolution. *Nano Letters* 2019; **19(6)**, 3569-3574.

[17] X Guo, T Liang, D Zhang, M Zhang, Y Lin and C Lai. Facile fabrication of 3D porous nickel networks for electro-oxidation of methanol and ethanol in alkaline medium. *Materials Chemistry and Physics* 2019; **221**, 390-396.

[18] F Nasirpouri. *Electrodeposited nanocrystalline films and coatings*. *In*: Electrodeposition of nanostructured materials. Springer, Cham, Switzerland, 2017, p. 261-288.

[19] S Cherevko, X Xing and CH Chung. Hydrogen template assisted electrodeposition of sub-micrometer wires composing honeycomb-like porous Pb films. *Applied Surface Science* 2011; **257(18)**, 8054-8061.

[20] W Zhang, C Ding, A Wang and Y Zeng. 3-D network pore structures in copper foams by electrodeposition and hydrogen bubble templating mechanism. *Journal of The Electrochemical Society* 2015; **162(8)**, D365.

[21] HM Rietveld. Line profiles of neutron powder-diffraction peaks for structure refinement. *Acta Crystallographica* 1967; **22**, 151-152.

[22] L Lutterotti. Maud: A Rietveld analysis program designed for the internet and experiment integration. *Acta Crystallographica Section A Foundations of Crystallography* 2000; **56(S1)**, s54.

[23] HM Rietveld. A profile refinement method for nuclear and magnetic structures. *Journal of Applied Crystallography* 1969; **2(2)**, 65-71.

[24] S Eugénio, TM Silva, MJ Carmezim, RG Duarte and MF Montemor. Electrodeposition and characterization of nickel-copper metallic foams for application as electrodes for supercapacitors. *Journal of Applied Electrochemistry* 2014; **44**, 455-465.

[25] M Kumar and NP Shetti. Magnetron sputter deposited NiCu alloy catalysts for production of hydrogen through electrolysis in alkaline water. *Materials Science for Energy Technologies* 2018; **1**, 160-165.

[26] F Chouikh, Y Beggah and MS Aida. Optical and electrical properties of Bi doped ZnO thin films deposited by ultrasonic spray pyrolysis. *Journal of Materials Science: Materials in Electronics* 2011; **22(5)**, 499-505.

[27] AA Akl, SA Mahmoud, SM Al-Shomar and AS Hassanien. Improving microstructural properties and minimizing crystal imperfections of nanocrystalline Cu_2O thin films of different solution molarities for solar cell applications. *Materials Science in Semiconductor Processing* 2018; **74**, 183-92.

[28] Z Jamil, E Ruiz-Trejo and NP Brandon. Nickel electrodeposition on silver for the development of solid oxide fuel cell anodes and catalytic membranes. *Journal of The Electrochemical Society* 2017; **164(4)**, D210-D217.

[29] Ö Söğüt, Ç Dönük, G Apaydın and ÖF Bakkaloğlu. Examination of CoNiCu thin films by using XRF and XRD. *Canadian Journal of Physics* 2014; **92(5)**, 435-439.

[30] WS Choi, HR Jung, SH Kwon, JW Lee, M Liu and HC Shin. Nanostructured metallic foam electrodeposits on a nonconductive substrate. *Journal of Materials Chemistry* 2012; **22(3)**, 1028-1032.

[31] C Miao, G Zhou, S Chen, H Xie and X Zhang. Synergistic effects between Cu and Ni species in $NiCu/\gamma\text{-}Al_2O_3$ catalysts for hydrodeoxygenation of methyl laurate. *Renewable Energy* 2020; **153**, 1439-1454.

[32] Y Li, G Huang, X Yin, X Chen, X Ma, Y Li and E Yao. Effect of copper ion concentration on microstructure and mechanical properties of electrolytic copper foil. *IOP Conference Series: Materials Science and Engineering* 2018; **381**, 12166.

[33] P Nath, R Pandey, A Das and A Mallik. Effect of deposition potential and copper concentration on the phase transformation mechanism and structural distribution during electrodeposition of Ni-Cu magnetic alloy thin films. *Metallic Materials* 2017; **55(4)**, 255-265.

[34] H An, NJ Siambun, BL Chuab, MGJ Hong and H Li. Structure transition mechanism in undercooled CuNi alloys. *Journal of Wuhan University of Technology, Materials Science Edition* 2021; **36**, 880-883.

[35] K Wasa, M Kitabatake and H Adachi. *Thin film materials technology: Sputtering of compound materials*. William Endrew Inc. Publishing, New York, 2004.

[36] Y Keereeta, W Panthuwat, T Suriwong, R Sirirak, A Prasatkhetragarn, C Boonruang and A Klinbumrung. Phase transition and optical characteristics of Mg doped $CuAlO_2$ synthesized

by facile thermal decomposition process. *Optik* 2022; **268**, 169840.

[37] Z Liu, X Xu, J Fang, X Zhu, J Chu and B Li. Microemulsion synthesis, characterization of bismuth oxyiodine/titanium dioxide hybrid nanoparticles with outstanding photocatalytic performance under visible light irradiation. *Applied Surface Science* 2012; **258(8)**, 3771-3778.

[38] Y Wu, JD Fowlkes and PD Rack. The optical properties of Cu-Ni nanoparticles produced via pulsed laser dewetting of ultrathin films: The effect of nanoparticle size and composition on the plasmon response. *Journal of Materials Research* 2011; **26(2)**, 277-287.

[39] HH Hsieh, YK Chang, WF Pong, JY Pieh, PK Tseng, TK Sham, I Coulthard, SJ Naftel, JF Lee, SC Chung and KL Tsang. Electronic structure of Ni-Cu alloys: The *d*-electron charge distribution. *Physical Review B* 1998; **57**, 15204.

[40] A Arman, T Ghodselahi, M Molamohammadi, S Solaymani, H Zahrabi and A Ahmadpourian. Microstructure and optical properties of Cu@Ni nanoparticles embedded in a-C:H. *Protection of Metals and Physical Chemistry of Surfaces* 2015; **51**, 575-578.

[41] S Goudarzi and V Dalouji. The effect of Cu content in MWCNTs synthesized by Ni-Cu@a-C:H catalyst on the optical constants and the optical loss. *Optik* 2020; **223**, 165585.

[42] AS Hassanien and AA Akl. Influence of composition on optical and dispersion parameters of thermally evaporated non-crystalline $Cd_{50}S_{50-x}Se_x$ thin films. *Journal of Alloys and Compounds* 2015; **648**, 280-290.

[43] AS Hassanien and AA Akl. Effect of Se addition on optical and electrical properties of chalcogenide CdSSe thin films. *Superlattices and Microstructures* 2016; **89**, 153-169.

[44] MA Ditta, MA Farrukh, S Ali and N Younas. X-ray peak profiling, optical parameters and catalytic properties of pure and CdS doped ZnO-NiO nanocomposites. *Russian Journal of Applied Chemistry* 2017; **90**, 151-159.

[45] KN Manjunatha and S Paul. Investigation of optical properties of nickel oxide thin films deposited on different substrates. *Applied Surface Science* 2015; **352**, 10-15.

[46] YH Liu, JC Zuo, XF Ren and L Yong. Synthesis and character of cerium oxide (CeO_2) nanoparticles by the precipitation method. *Metalurgija* 2014; **53(4)**, 463-465.